

Research Article

Marwan Gebran^{1*}, Frédéric Paletou², Ian Bentley¹, Rose Brienza¹, and Kathleen Connick¹

Deep Learning application for stellar parameters determination: II- Application to observed spectra of AFGK stars

DOI: DOI

Received ..; revised ..; accepted ..

Abstract: In this follow-up paper, we investigate the use of Convolutional Neural Network for deriving stellar parameters from observed spectra. Using hyperparameters determined previously, we have constructed a Neural Network architecture suitable for the derivation of T_{eff} , $\log g$, $[M/H]$, and $v_e \sin i$. The network was constrained by applying it to databases of AFGK synthetic spectra at different resolutions. Then, parameters of A stars from Polarbase, SOPHIE, and ELODIE databases are derived as well as FGK stars from the Spectroscopic Survey of Stars in the Solar Neighbourhood. The network model average accuracy on the stellar parameters are found to be as low as 80 K for T_{eff} , 0.06 dex for $\log g$, 0.08 dex for $[M/H]$, and 3 km/s for $v_e \sin i$ for AFGK stars.

Keywords: methods: data analysis, methods: statistical, methods: deep learning, techniques: spectroscopic, stars: fundamental parameters.

1 Introduction

Artificial Intelligence (AI) is becoming a vital tool in science due to its automation capabilities and its capacity to handle large amounts of data. In the context of astronomy, a subset of AI, Machine and Deep Learning (ML and DL) are used extensively for ground-based and sky surveys (Baron, 2019). In our previous work, Gebran et al. (2022) (hereafter referred to as Paper I), we constructed a Deep Neural Network (DNN) in order to derive stellar parameters¹ such as: effective temperature (T_{eff}), surface gravity ($\log g$), metallicity ($[M/H]$), and the projected equatorial rotational velocity ($v_e \sin i$) for B and A stars. In Paper I, we constrained most of the hyperparameters utilized in the construction of the Neural Network (NN) in order to insure that the best accuracy for deriving stellar labels could be achieved.

Many tools and techniques are being developed to derive the fundamental parameters of stars and most of them are either based on statistical or ML/DL approaches. A thorough list of the most updated studies can be found in the introduction of Paper I. Recently, Li et al.

(2022b) used a combination of Least Absolute Shrinkage and Selection Operator (LASSO) and Multi-layer Perceptron (MLP) methods to estimate stellar atmospheric parameters from the Large Sky Area Multi-Object Fiber Spectroscopic Telescope (LAMOST) DR8 low-resolution spectra. Straumit et al. (2022) presented a spectral analysis algorithm, ZETA-PAYNE, developed to obtain stellar labels from SDSS-V spectra of stars of OBAF spectral types using machine learning tools. Li et al. (2022a) applied a ML technique, the Gaussian Process (GP) regression, to turn a sparse model grid into a continuous function. They also used the GP regression to determine the age and mass of stars. Kjærsgaard et al. (2021) presented a neural network autoencoder approach for extracting a telluric transmission spectrum from a large set of high-precision observed solar spectra from the The High Accuracy Radial Velocity Planet Searcher (HARPS-N) radial velocity spectrograph. Hu et al. (2022) presented a data-driven method based on long short-term memory (LSTM) neural networks to analyze spectral time series of Type Ia supernovae (SNe Ia). Their method allows for accurate reconstruction of the spectral sequence of an SN Ia based on a single observed spectrum around maximum light. More recently, Xiong et al. (2022) presented a Residual Recurrent Neural Network (RRNet) to extract spectral information, and estimate stellar atmospheric parameters

¹ When dealing with DNN, stellar parameters are often called stellar labels.

along with 15 chemical element abundances for medium-resolution spectra from LAMOST.

Most of the automated techniques that are found in the literature deal with the derivation of the fundamental parameters (T_{eff} , $\log g$, $[M/H]$) without considering $v_e \sin i$. Rotational profiles are usually found by applying transformations such as the Fourier Transform (FT, Zorec and Royer 2012) or using rotational laws (Zorec et al., 2017). In our previous studies (Aydi et al., 2014; Gebran et al., 2016; Kassounian et al., 2019; Gebran et al., 2022), we have derived $v_e \sin i$ using line profile fitting.

In this work, we complement the study of Paper I by using its best combination of hyperparameters to find the best NN architecture. The foremost purpose of our study is to develop a consistent model that is capable of predicting accurate and precise stellar parameters which is a guiding starting point to most stellar physics projects. Of course other sources of uncertainties can affect the predicted results when applied to real observations as will be discussed in this paper. Once the architecture and parameters are set, our technique is then applied to AFGK observed spectra (Gebran et al., 2016; Kassounian et al., 2019; Paletou et al., 2015).

The construction of the training databases is explained in Sec. 2. The pre-processing steps are detailed in Sec. 3. The construction of the NN model with all the details are discussed in Sec. 4. The application of the method to AFGK stars is found in Secs. 5. The discussion and conclusion can be found in Sec. 6.

2 Training Databases

A grid of 12 training databases was constructed for the purpose of this study. Other than modifying the stellar labels (T_{eff} , $\log g$, $[M/H]^2$, $v_e \sin i$), we have constructed a series of grids with the same range of stellar labels but at different resolving power. The purpose is to analyse the effect of resolution on the accuracy of the derived stellar label and to check the capability of our technique when applied to low, medium, and high resolution spectrometers.

We have followed the same strategy as in Paper I. We have first calculated a series of ATLAS9 (Kurucz, 1992) model atmospheres using the opacity distribution function of Castelli and Kurucz (2003) and with a mixing

length parameter of 0.5 for $7000 \text{ K} \leq T_{\text{eff}} \leq 8500 \text{ K}$, and 1.25 for $T_{\text{eff}} \leq 7000 \text{ K}$ (Smalley, 2004). Using SYNSPEC48 (Hubeny and Lanz, 1992), we have calculated synthetic spectra for AFGK stars. We ended up, for each resolving power, with a grid of 80 000 synthetic spectra with parameters ranging randomly between the values described in Tab. 1. We have used the same line list as the one used in Paper I. The wavelength range was selected to be between 4450 and 5400 Å. This wavelength range is indeed very sensitive to all stellar parameters in the spectral range of AFGK stars (Paletou et al., 2015; Gebran et al., 2016; Kassounian et al., 2019; Gebran et al., 2022). This region is also insensitive to microturbulent velocity which was adopted to be $\xi_t = 2 \text{ km/s}$ for A stars and $\xi_t = 1 \text{ km/s}$ for FGK stars (Gebran et al., 2016, 2014). A example of the calculated spectra for different resolving powers is displayed in Fig. 1.

3 PCA for Pre-processing

Before applying the NN to the training database, a dimension reduction technique is applied. This step consists in reducing the size of the spectra from a sampling size of N_λ to $n_k < N_\lambda$. Depending on the resolving power, N_λ ranges between 4 750 to 19 000 data points. The n_k reduced data points are found by projecting the flux of each spectrum onto the first 50 Principal Components (PC). Technically, we apply this Principal Component Analysis (PCA) on the training database and we find the eigenvectors $\mathbf{e}_k(\lambda)$ of the variance-covariance matrix \mathbf{C} :

$$\mathbf{C} = (\mathbf{M} - \bar{\mathbf{M}})^T \cdot (\mathbf{M} - \bar{\mathbf{M}}), \quad (1)$$

where the training database \mathbf{M} is a $N_{\text{spectra}} \times N_\lambda$ matrix containing the fluxes of the synthetic spectra. The value of n_k is found by analyzing the reconstructed error (Gebran et al., 2022). Having $n_k=50$ reduces the mean reconstructed error to a value less than 0.5%. As a similar technique to PCA, one could also use the encoder part of an autoencoder in order to reduce the dimensionality of the database (Kjærsgaard et al., 2021). We have chosen PCA to be consistent with our previous findings in Gebran et al. (2016) and Gebran et al. (2022).

4 Deep Learning

We start by applying data augmentation as a regularization technique to all the training databases (see Sec. 4.1.1

2 $[M/H]$ refers to an overall metallicity and not to the iron abundance. All elemental abundances are scaled according to $[M/H]$.

Table 1. Ranges of the parameters used for the calculation of the training databases. The 3rd column displays the steps in the parameter range. Note that the steps in T_{eff} and $\log g$ are the steps in ATLAS9 model atmospheres. Many databases were constructed for different resolving power ranging from 1 000 to 115 000. Random steps means that there is no restriction on the number selection.

Parameters	Range	Step
T_{eff} (K)	[4 000,11 000]	50
$\log g$ (dex)	[2.0, 5.0]	0.05
$[M/H]$ (dex)	[-1.5, 1.5]	random
$v_e \sin i$ (km s ⁻¹)	[0, 300]	random
λ (Å)	4 450-5 400	λ
		Resolving Power

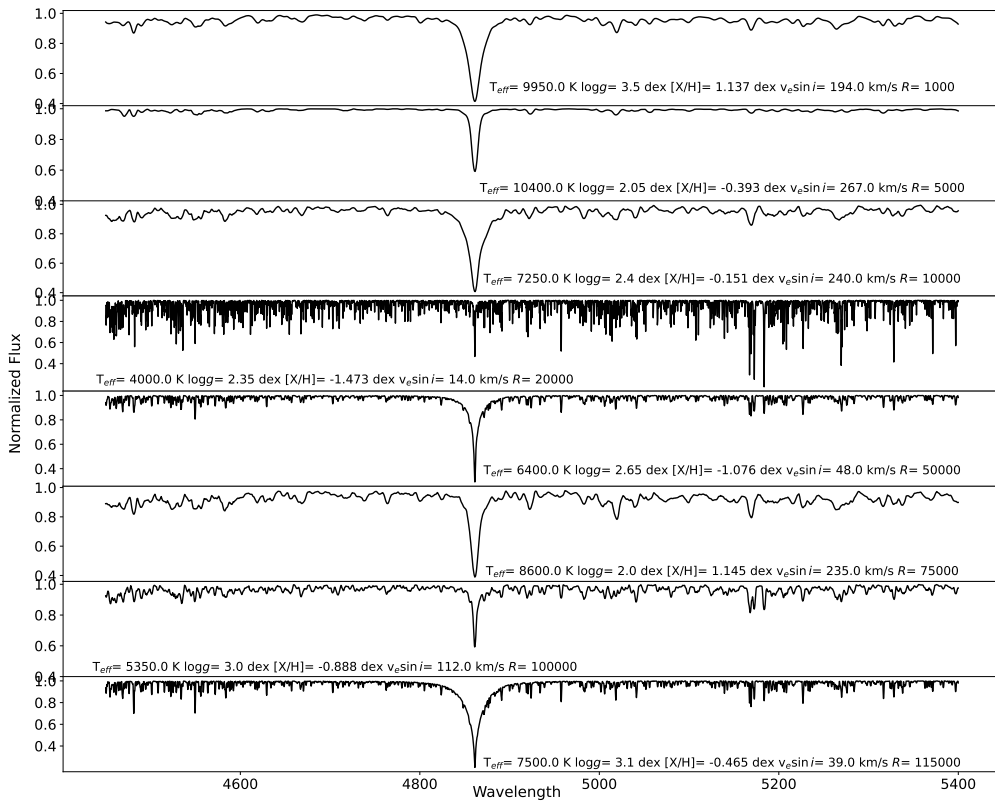


Fig. 1. Sample of synthetic spectra calculated with different stellar parameters and spectral resolutions. These noise free spectra are normalized to the local continuum.

of Paper I for technical explanations). This is done in order to take into account the noise in the real observed spectra as well as considering some modifications that could occur in the shape of the observed spectra due to a bad normalization or inappropriate data reduction. Every spectrum (including the augmented ones) in each

database is represented by 50 data points and they correspond to a specific T_{eff} , $\log g$, $[M/H]$, and $v_e \sin i$. This is true at all resolving powers. A NN is then used to link these data points to their corresponding labels. Four different NNs were built, one for each stellar label (T_{eff} , $\log g$, $[M/H]$, $v_e \sin i$).

The initializers, optimizers, learning rates, dropout fraction, pooling layers, activation functions, loss functions, epochs, and batches are constrained according to the methodology of Paper I. These network parameters were derived for every network architecture tested in this work.

4.1 Architecture

An infinite number of architectures could be applied to our purpose. The main goal is to find the most accurate transformation between the matrix of spectra coefficients (the 50 projected ones) and the labels. The best architecture will be selected according to its simplicity (size and calculation time) and to the accuracy of the results.

Fully dense NNs, Convolutional Neural Networks (CNN), and a combination of both were tested for each stellar label. In each case we have iterated on the number of layers, number of neurons in each layer, and the size of the filters in case of CNNs. As explained previously, network parameters were derived for each NN.

For every network and every resolving power, each augmented database was divided in 70% for training, 20% for validation, and 10% for testing. Gaussian signal to noise ratio (SNR) was selected randomly between 5 and 300 and applied to each spectrum of the 10% test spectra in order to check the accuracy of the technique on noisy data.

All our calculations are performed using the open-source programming language, Python, specifically with the Keras³ interface on the TensorFlow TensorFlow⁴. We have used the KerasTuner⁵ package (O’Malley et al., 2019), a scalable hyperparameter optimization framework that solves the pain points of hyperparameter search. It was used to derive the optimized number of layers as well as the filter sizes in case of CNNs. Linking the number of layers and dimension of the filters with the size of the database as well as the size of each spectrum in the database is not an easy task. In order to avoid over- and under-fitting, these two parameters should be optimized. KerasTuner helps in that regard and avoids the hassle of the time consuming trial and error phase.

After iterating the architecture shape and deriving the optimized parameters for each network, the result was a unique architecture that is applicable to all stellar parameters. Figure 2 shows the architecture of NN for

deriving T_{eff} . This architecture is similar for predicting $\log g$, $[M/H]$, and $v_e \sin i$. Although the four parameters are predicted with networks having similar architecture, these models differ in the activation function, the kernel initializer, the loss function, the optimizer, the dropout fraction, the epochs and the batches number (Gebran et al., 2022). The adopted values for the network parameters are derived using the technique explained in Paper I. These parameters are summarized in Tab. 2.

4.2 Resolution Effect

Spectroscopic surveys are based on instruments that have different resolving power. For that reason, we have applied our technique to different databases that are similar in parameter ranges (Tab. 1), except for the resolving power. Our tests contain spectra having a low resolution down to 1 000 and a high resolution up to 115 000.

Once the networks are trained using the 70% of the data, we have derived the accuracy on the parameters for the validation, test, and noisy test data. The best accuracy reached as a function of the resolution are displayed in Fig. 3. For each stellar label, the derived accuracy for the noisy test data is representative of the error bar that should be assigned to observed spectra. For example, analyzing spectra at a resolving power of 50 000, the equatorial projected rotational velocity should be assigned and error $\sigma_{v_e \sin i_m} \sim 2.5$ km/s. The subscript m corresponds to the fact that this is model related. For a resolving power larger than 5 000, the accuracy’s are always in the same order and their average is 80 K for T_{eff} , 0.06 dex for $\log g$, 0.08 dex for $[M/H]$, and 3 km/s for $v_e \sin i$.

5 Application to Observed Spectra

After the four networks were applied to synthetic data and the architecture and parameters found, we used them to predict the stellar parameters from *observed* spectra. We used well studied AFGK stars observed with different instruments at different resolution. Applying the predictions to observed spectra assumes that the radiative transfer code is able to produce synthetic spectra similar to the observed ones using the specific stellar parameters. We have shown in previous studies (Gebran et al., 2016; Kassounian et al., 2019) that SYNSPEC48 was able to reproduce spectra of AFGK stars with good accuracy but other reliable synthetic spectra codes could be used

³ <https://keras.io/>

⁴ <https://www.tensorflow.org/>

⁵ https://keras.io/keras_tuner/

Table 2. Set of parameters used for the 4 networks, for deriving T_{eff} , $\log g$, $[M/H]$, and $v_e \sin i$. These parameters are derived using the technique explained in Paper I.

Parameter	T_{eff}	$\log g$	$[M/H]$	$v_e \sin i$
Kernel initializer	he_normal	he_normal	Random Uniform	he_uniform
Loss function	mean squared logarithmic error	mean squared logarithmic error	mean absolute error	mean squared error
Optimizer	Adam	Adamax	Adam	Adamax
Epochs	350	75	75	75
Batch	128	128	32	64
Activation function	Relu	tanh	tanh	tanh
Dropout fraction	0.3	0.3	0.2	0.3

if needed. We can mention the PHOENIX models (Husser et al., 2013) that are well suited for stars having $T_{\text{eff}} \leq 12\,000$ K or TURBOSPECTRUM (Plez, 2012) with all the molecular data that is used for giants and dwarfs stars.

For the A stars, we used the list of Gebran et al. (2016) and selected the ones that have the most values published in the literature. We ended up with 89 observed A stars with more than 9 values for T_{eff} in the Vizier catalog. These A stars were observed with NARVAL and ESPaDOnS high-resolution spectropolarimeters and having a spectral resolving power of 65 000 in polarimetric mode and 76 000 when used for spectroscopy. These spectra were retrieved from PolarBase (Petit et al., 2014), a high resolution spectropolarimetric stellar observations database. Another part of the A stars spectra were observed with ELODIE (Baranne et al., 1996) and SOPHIE (Perruchot et al., 2011) spectrographs with a resolving power of 42 000 and 75 000, respectively. Details about the observations can be found in Gebran et al. (2016) and Kassounian et al. (2019). For the FGK stars, we have used 96 stellar spectra from the Spectroscopic Survey of Stars in the Solar Neighbourhood (S^4N , Allende Prieto et al. 2004), analysed in Paletou et al. (2015) having a resolving power of 50 000. Like done in our previous studies (Paletou et al., 2015; Gebran et al., 2016), variable or active stars, showing at time emission features of changing strength/amplitude were excluded.

For each resolving power, we used the corresponding trained NN model. To do that, the observations were corrected for the radial velocity shift using the classical cross correlation technique (Tonry and Davis, 1979). The spectra are then interpolated in the wavelength range used during the training, between 4450 and 5400 Å for A stars and 5000 to 5400 Å for FGK stars. The wavelength range of the S^4N observations is smaller than that of A stars. For that reason, a reduced database with smaller wavelength range was interpolated from the original one at 50 000 resolving power, and was used for these specific FGK stars. Then all observed spectra were projected into

their corresponding principal components and the first 50 data points were conserved for the prediction.

5.1 AFGK Stars

Predicted stellar parameters are depicted in Tabs. 4 and 5 in the appendix. In these tables, the stellar parameters are represented with the median and closest values retrieved from Vizier catalogues using astroquery⁶ (Paletou and Zolotukhin, 2014)⁷.

Figure 4 shows the predicted effective temperature of a sample of stars as well as the range in the effective temperatures retrieved from the catalogues (box-plots) and the median. The selection of these stars was based on the number of values found in the literature. For A stars, we have selected the ones that have more than 20 different values in Vizier. As for FGK stars, we did the same with stars having more than 100 independent literature values for T_{eff} . Figures 5 to 7 are similar to Fig. 4 but for $\log g$, $[M/H]$, and $v_e \sin i$. A stars in Fig. 5 have more than 10 catalogued values for $\log g$ and F stars have more than 50. For $[M/H]$ and $v_e \sin i$, we have chosen the A stars that have more than 10 catalogued values for these two parameters. For FGK stars, we have selected the ones having more than 50 and 15 values for $[M/H]$ and $v_e \sin i$, respectively.

A large spread exists in the literature values for all parameters. To estimate the accuracy of our results, we used a weighted mean approach similar to the one described in Gebran et al. (2016). Quantitatively, and in order to give more weight to the catalogued values that have a large number of occurrence and a small spread in values, the dispersion and its corresponding standard deviation for a stellar parameter X are calculated as follows:

$$\Delta X = \frac{\sum_i w_i (X^{\text{prediction}} - X^{\text{median}})}{\sum_i w_i}$$

⁶ <https://astroquery.readthedocs.io>

⁷ <https://arxiv.org/abs/1408.7026>

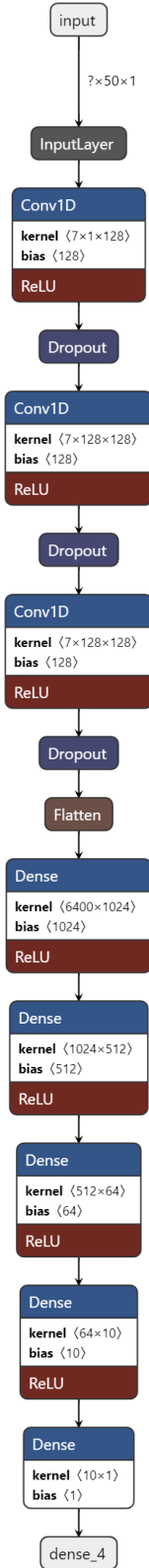


Fig. 2. Neural Networks architecture used in this study. The parameters displayed in this model are the ones used for predicting T_{eff} , $\log g$, $[M/H]$, and $v_e \sin i$ are predicted with networks having the same architecture but different parameters as shown in Tab. 2. Explanations about the kernel and bias dimensions can be found in Wu (2017).

where

$$w_i = \frac{1}{\text{IQR}_i}$$

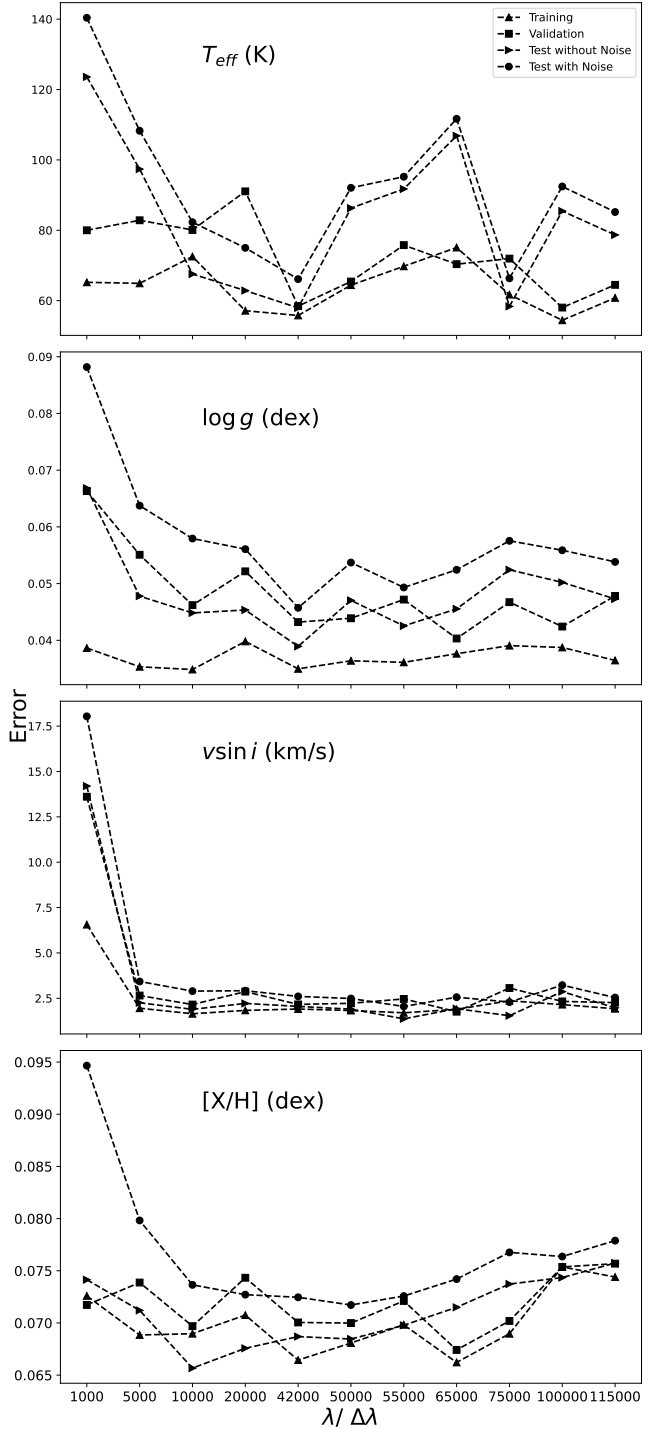


Fig. 3. Derived accuracy for T_{eff} , $\log g$, $[M/H]$, and $v_e \sin i$ as a function of the resolving power. We present the accuracy's for the training data (triangles), the validation (squares), test (triangles tilted right), and noisy test (circles) data.

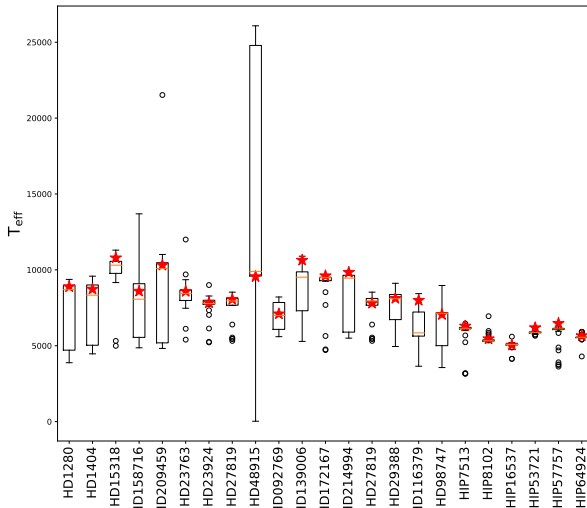


Fig. 4. Comparison between our predicted effective temperatures (stars), and the values we obtained from available Vizier catalogues. The catalogued values are represented as classical boxplots. Objects we studied are listed along the horizontal axis. The horizontal bar inside each box indicates the median (Q₂ value), while each box extends from first quartile, Q₁, to third quartile Q₃. Extreme values, still within a 1.5 times the interquartile range away from either Q₁ or Q₃, are connected to the box with dashed lines. Outliers are denoted by a “o” symbol.

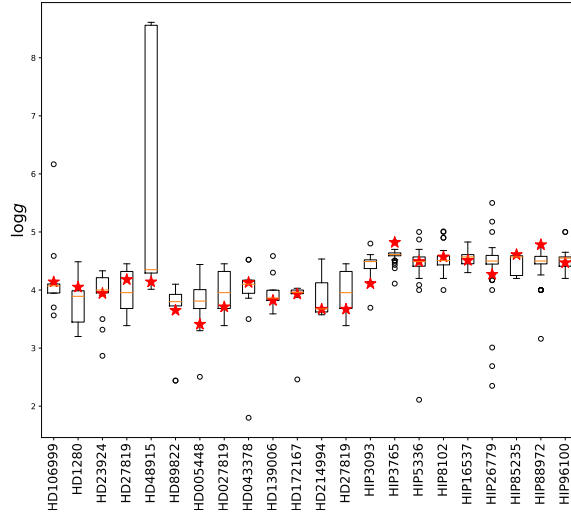


Fig. 5. Same as Fig. 4 but for $\log g$.

IQR_i being the interquartile range defined as the difference between the third and first quartile of each set of values. The standard deviation is calculated as:

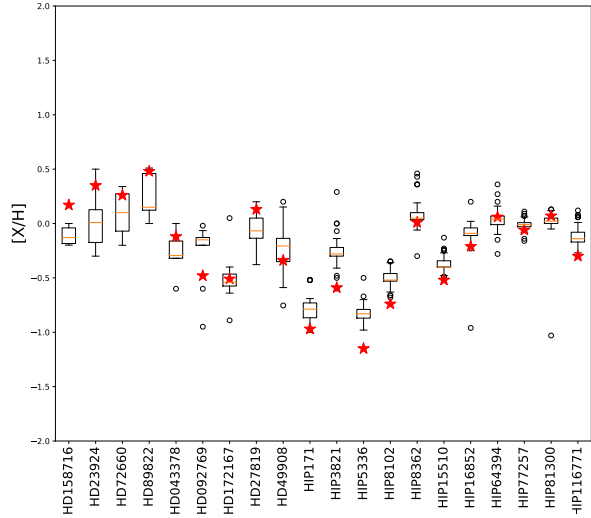


Fig. 6. Same as Fig. 4 but for $[M/H]$.

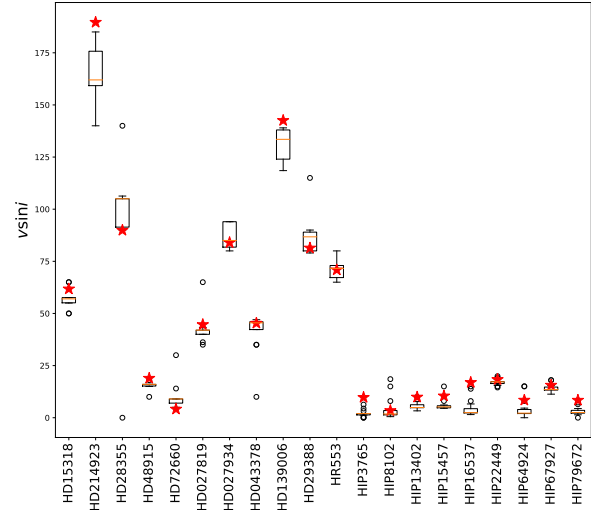


Fig. 7. Same as Fig. 4 but for $v_e \sin i$.

$$\sigma_X = \sqrt{\frac{\sum_i w_i (X^{\text{prediction}} - X^{\text{median}})^2}{\sum_i w_i}}$$

Stars having only one catalogued value for a specific parameter were not considered in the calculation of the dispersion. The results of the dispersion as well as the standard deviations are displayed in Tab. 3. Catalogued values are all coming from different sources and each author uses a different technique (photometry, spectroscopy, spectrophotometry, asteroseismology...). This leads to a

	T_{eff} (K)	$\log g$ (dex)	[M/H] (dex)	$v_e \sin i$ (km/s)
Δ	160	0.40	0.15	12
σ	300	0.55	0.35	15
Δ_{lim}	150	0.01	0.04	3.0
σ_{lim}	250	0.15	0.14	5.5

Table 3. Dispersion and standard deviation for the comparison between our predicted parameters and the catalogued ones. The last two rows deals with a limited catalogued sample, the one used to plot Figs. 4 to 7.

large dispersion and a large deviation between our predicted values and the ones in the literature. A better way to estimate this dispersion is to do the comparison with the sample used in Figs. 4 to 7. This sample contains the stars having the largest number of independent catalogued values. The new dispersion and standard deviations are displayed in Tab. 3 depicted with the "lim" subscript. In that case, the dispersion reduces drastically, reaching an average of 150 K, 0.01 dex, 0.04 dex, and 3.0 km/s for T_{eff} , $\log g$, [M/H], and $v_e \sin i$, respectively and with smaller standard deviation than in the case of the whole sample.

The dispersion found between our predicted $v_e \sin i$ for FGK and the ones in the literature are mainly explained by the fact that our $v_e \sin i$ include the macroturbulence effects whereas some of the authors derive both parameters separately (see for example Allende Prieto et al. 2004). In the case of A stars, the $v_e \sin i$ values for very sharp-lined spectra (e.g., $v_e \sin i \leq 5$ km/s) should be considered as upper limits because macroturbulence effect is neglected. For moderate and fast rotators, macroturbulence has no significant effect on the line shape (Takeda et al., 2018; Frémat et al., 2022). When only considering A stars, Δ_{lim} and σ_{lim} of Tab. 3 become 1.3 km/s and 5.0 km/s, respectively. These results show that we are able to recover the stellar parameters of AFGK stars with good accuracy using our trained models. However, as explained in Paper I, the size of the database is very crucial for the convergence of the model as well as for the recovered accuracy of the stellar parameter. The size of the database depends on many factors, the spectral type of the stars, the wavelength range and the type of predicted parameters. We have used a database of $\sim 80\,000$ spectra in our study but this number should be monitored.

6 Discussion and Conclusion

Two sources of errors should be assigned to the predicted stellar parameters. One relates to the model ($\sigma_{\text{parameter}_m}$, Sec. 4.2) and the other relates to how close the radiative transfer code (*i.e.* SYNSPEC48, $\sigma_{\text{parameter}_{\text{rtc}}}$) represents the observations. $\sigma_{\text{parameter}_{\text{rtc}}}$ can be derived using a list of well studied stars with well established stellar parameters over a wide range in the HR Diagram. It is beyond the scope of this study, but we should be aware that this source of error could be wavelength dependant as each radiative transfer code uses a different line list with different atomic data.

Model (*i.e* NN) and radiative transfer errors are independent and can be added in quadratic manner to find the total accuracy that we found in Sec. 5.1:

$$\sigma_{\text{parameter}_{\text{total}}} = (\sigma_{\text{parameter}_m}^2 + \sigma_{\text{parameter}_{\text{rtc}}}^2)^{\frac{1}{2}}$$

While comparing with the median values from literature, we found that T_{eff} is derived with an accuracy of 150 K, $\log g$ with 0.01 dex, [M/H] with 0.04 dex, and $v_e \sin i$ with 3.0 km/s. Some of these deviations are smaller than the errors found in the model (80 K for T_{eff} , 0.06 dex for $\log g$, 0.08 dex for [M/H], and 3.0 km/s for $v_e \sin i$), but one should consider the accuracy of the model as a minimum limit for the stellar parameters and then calculate the total accuracy depending on the radiative transfer code specificity.

We have used a large range of spectral type and found acceptable values for the accuracy. One could use a combination of stellar library with synthetic data adapted for each spectral type and luminosity range or a large database of observed stars with accurate stellar parameters. However, NN prove to be a fast (*refer to Paper I for computational time*) and accurate way to derive stellar parameters and can handle a large amount of data. These results are very promising as they are less than the accuracy that are usually found with photometric techniques (Smalley, 2005; Jin-Meng et al., 2021; Green et al., 2021) or spectroscopic ones (Gill et al., 2018; Gebran et al., 2016; Ting et al., 2019; Kassounian et al., 2019; Tabernero et al., 2022) or a combination of both (Adelman et al., 2002; Heiter et al., 2015).

In a future work, we will be testing the effect of specific spectral region on the stellar parameters. This will be done through autoencoders, a type of unsupervised learning technique, leading to a more "intelligent" and compact database construction.

One straightforward application is the use of such a network in order to derive the stellar parameters of

Gaia spectra (Gaia Collaboration et al., 2016). The radial velocity spectrometer (RVS, Cropper et al. 2018) on board of Gaia will deliver medium resolution spectra ($R \sim 11\,000$) in the CaII triplet region (λ ranging from 8470 to 8710 Å). Several millions of stars have their spectra available during the Data Release 3 (DR3, Gaia Collaboration et al. 2022; Frémat et al. 2022).

Acknowledgment: We are very grateful to the referees of the paper for the useful remarks.

Funding information: This work was supported by the Neuhoff Summer Research Scholarship program at Saint Mary’s College.

Author contributions: All authors have accepted responsibility for the entire content of this manuscript and approve edits submission.

Conflict of interest: The authors state no conflict of interest.

References

- Adelman, S. J., Pintado, O. I., Nieva, M. F., Rayle, K. E., and Sanders, S. E., J. (2002). On the effective temperatures and surface gravities of superficially normal main sequence band B and A stars. *A & A*, 392:1031–1037.
- Allende Prieto, C., Barklem, P. S., Lambert, D. L., and Cunha, K. (2004). S⁴N: A spectroscopic survey of stars in the solar neighborhood. The Nearest 15 pc. *A & A*, 420:183–205.
- Aydi, E., Gebran, M., Monier, R., Royer, F., Lobel, A., and Blomme, R. (2014). Automated procedure to derive fundamental parameters of B and A stars: Application to the young cluster NGC 3293. In Ballet, J., Martins, F., Bournaud, F., Monier, R., and Reylé, C., editors, *SF2A-2014: Proceedings of the Annual meeting of the French Society of Astronomy and Astrophysics*, pages 451–455.
- Baranne, A., Queloz, D., Mayor, M., Adrianzyk, G., Knispel, G., Kohler, D., Lacroix, D., Meunier, J.-P., Rimbaud, G., and Vin, A. (1996). Elodie: A spectrograph for accurate radial velocity measurements. *Astron. Astrophys. Suppl. Ser.*, 119(2):373–390.
- Baron, D. (2019). Machine Learning in Astronomy: a practical overview. *arXiv e-prints*, page arXiv:1904.07248.
- Castelli, F. and Kurucz, R. L. (2003). New Grids of ATLAS9 Model Atmospheres. In Piskunov, N., Weiss, W. W., and Gray, D. F., editors, *Modelling of Stellar Atmospheres*, volume 210, page A20.
- Cropper, M., Katz, D., Sartoretti, P., Prusti, T., de Bruijne, J. H. J., Chassat, F., Charvet, P., Boyadjian, J., Perryman, M., Sarri, G., Gare, P., Erdmann, M., Munari, U., Zwitter, T., Wilkinson, M., Arenou, F., Vallenari, A., Gómez, A., Panuzzo, P., Seabroke, G., Allende Prieto, C., Benson, K., Marchal, O., Huckle, H., Smith, M., Dolding, C., Janßen, K., Viala, Y., Blomme, R., Baker, S., Boudreault, S., Crifo, F., Soubiran, C., Frémat, Y., Jasniewicz, G., Guerrier, A., Guy, L. P., Turon, C., Jean-Antoine-Piccolo, A., Thévenin, F., David, M., Gosset, E., and Damerdji, Y. (2018). Gaia Data Release 2. Gaia Radial Velocity Spectrometer. *A & A*, 616:A5.
- Frémat, Y., Royer, F., Marchal, O., Blomme, R., Sartoretti, P., Guerrier, A., Panuzzo, P., Katz, D., Seabroke, G. M., Thévenin, F., Cropper, M., Benson, K., Damerdji, Y., Haigron, R., Lobel, A., Smith, M., Baker, S. G., Chemin, L., David, M., Dolding, C., Gosset, E., Janßen, K., Jasniewicz, G., Plum, G., Samaras, N., Snaith, O., Soubiran, C., Vanel, O., Zorec, J., Zwitter, T., Brouillet, N., Caffau, E., Crifo, F., Fabre, C., Fragkoudi, F., Huckle, H. E., Lasne, Y., Leclerc, N., Mastrobuono-Battisti, A., Jean-Antoine Piccolo, A., and Viala, Y. (2022). Gaia Data Release 3: Properties of the line broadening parameter derived with the Radial Velocity Spectrometer (RVS). *arXiv e-prints*, page arXiv:2206.10986.
- Gaia Collaboration, Creevey, O. L., Sarro, L. M., Lobel, A., Pancino, E., Andrae, R., Smart, R. L., Clementini, G., Heiter, U., Korn, A. J., Fouesneau, M., Frémat, Y., De Angeli, F., Vallenari, A., Harrison, D. L., Thévenin, F., Reylé, C., Sordo, R., Garofalo, A., Brown, A. G. A., Eyer, L., Prusti, T., de Bruijne, J. H. J., Arenou, F., Babusiaux, C., Biermann, M., Ducourant, C., Evans, D. W., Guerra, R., Hutton, A., Jordi, C., Klioner, S. A., Lammers, U. L., Lindegren, L., Luri, X., Mignard, F., Panem, C., Pourbaix, D., Randich, S., Sartoretti, P., Soubiran, C., Tanga, P., Walton, N. A., Bailer-Jones, C. A. L., Bastian, U., Drimmel, R., Jansen, F., Katz, D., Lattanzi, M. G., van Leeuwen, F., Bakker, J., Cacciari, C., Castañeda, J., Fabricius, C., Galluccio, L., Guerrier, A., Masana, E., Messineo, R., Mowlavi, N., Nicolas, C., Nienartowicz, K., Pailler, F., Panuzzo, P., Riclet, F., Roux, W., Seabroke, G. M., Gracia-Abril, G., Portell, J., Teyssier, D., Altman, M., Audard, M., Bellas-Velidis, I., Benson, K., Berthier, J., Blomme, R., Burgess, P. W., Busonero, D., Busso, G., Cánovas, H., Carry, B., Cellino, A., Cheek, N., Damerdji, Y., Davidson, M., de Teodoro, P., Nuñez Campos, M., Delchambre, L., Dell’Oro, A., Esquej, P., Fernández-Hernández, J., Fraile, E., Garabato, D., García-Lario, P., Gosset, E., Haigron, R., Halbwachs, J. L., Hambly, N. C., Hernández, J., Hestroffer, D., Hodgkin, S. T., Holl, B., Janßen, K., Jevardat de Fombelle, G., Jordan, S., Krone-Martins, A., Lanzafame, A. C., Löffler, W., Marchal, O., Marrese, P. M., Moitinho, A., Muinonen, K., Osborne, P., Pauwels, T., Recio-Blanco, A., Riello, M., Rimoldini, L., Roegiers, T., Rybizki, J., Siopis, C., Smith, M., Sozzetti, A., Utrilla, E., van Leeuwen, M., Abbas, U., Ábrahám, P., Abreu Aramburu, A., Aerts, C., Aguado, J. J., Ajaj, M., Aldea-Montero, F., Altavilla, G., Álvarez, M. A., Alves, J., Anders, F., Anderson, R. I., Anglada Varela, E., Antoja, T., Baines, D., Baker, S. G., Balaguer-Núñez, L., Balbinot, E., Balog, Z., Barache, C., Barbato, D., Barros, M., Barstow, M. A., Bartolomé, S., Bassilana, J. L., Bauchet, N., Becciani, U., Bellazzini, M., Berihuete, A., Bernet, M., Bertone, S., Bianchi, L., Binnenfeld, A., Blanco-Cuaresma, S., Boch, T., Bombrun, A., Bossini, D., Bouquillon, S., Bragaglia, A., Bramante, L., Breedt, E., Bressan, A., Brouillet, N., Brugaletta, E., Bucciarelli, B., Burlacu, A., Butkevich, A. G., Buzzi, R.,

- Caffau, E., Cancelliere, R., Cantat-Gaudin, T., Carballo, R., Carlucci, T., Carnerero, M. I., Carrasco, J. M., Casamiquela, L., Castellani, M., Castro-Ginard, A., Chaoul, L., Charlot, P., Chemin, L., Chiaramida, V., Chiavassa, A., Chornay, N., Comoretto, G., Contursi, G., Cooper, W. J., Cornez, T., Cowell, S., Crifo, F., Cropper, M., Crosta, M., Crowley, C., Dafonte, C., Dapergolas, A., David, P., de Laverny, P., De Luise, F., De March, R., De Ridder, J., de Souza, R., de Torres, A., del Peloso, E. F., del Pozo, E., Delbo, M., Delgado, A., Delisle, J. B., Demouchy, C., Dharmawardena, T. E., Di Matteo, P., Diakite, S., Diener, C., Distefano, E., Dolding, C., Enke, H., Fabre, C., Fabrizio, M., Faigler, S., Fedorets, G., Fernique, P., Figueras, F., Fournier, Y., Fouron, C., Fragkoudi, F., Gai, M., Garcia-Gutierrez, A., Garcia-Reinaldos, M., García-Torres, M., Gavel, A., Gavras, P., Gerlach, E., Geyer, R., Giacobbe, P., Gilmore, G., Girona, S., Giuffrida, G., Gomel, R., Gomez, A., González-Núñez, J., González-Santamaría, I., González-Vidal, J. J., Granvik, M., Guillout, P., Guiraud, J., Gutiérrez-Sánchez, R., Guy, L. P., Hatzidimitriou, D., Hauser, M., Haywood, M., Helmer, A., Helmi, A., Sarmiento, M. H., Hidalgo, S. L., Hładcuk, N., Hobbs, D., Holland, G., Huckle, H. E., Jardine, K., Jasniewicz, G., Jean-Antoine Piccolo, A., Jiménez-Arranz, Ó., Juaristi Campillo, J., Julbe, F., Karbevska, L., Kervella, P., Khanna, S., Kordopatis, G., Kóspál, Á., Kostrzewska-Rutkowska, Z., Kruszyńska, K., Kun, M., Laizeau, P., Lambert, S., Lanza, A. F., Lasne, Y., Le Campion, J. F., Lebreton, Y., Lebzelter, T., Leccia, S., Leclerc, N., Lecoeur-Taibi, I., Liao, S., Licata, E. L., Lindstrøm, H. E. P., Lister, T. A., Livianou, E., Lorca, A., Loup, C., Madrero Pardo, P., Magdaleno Romeo, A., Managau, S., Mann, R. G., Manteiga, M., Marchant, J. M., Marconi, M., Marcos, J., Marcos Santos, M. M. S., Marín Pina, D., Marinoni, S., Marocco, F., Marshall, D. J., Polo, L. M., Martín-Fleitas, J. M., Marton, G., Mary, N., Masip, A., Massari, D., Mastrobuono-Battisti, A., Mazeh, T., McMillan, P. J., Messina, S., Michalik, D., Millar, N. R., Mints, A., Molina, D., Molinaro, R., Molnár, L., Monari, G., Monguió, M., Montegriffo, P., Montero, A., Mor, R., Mora, A., Morbidelli, R., Morel, T., Morris, D., Muraveva, T., Murphy, C. P., Musella, I., Nagy, Z., Noval, L., Ocaña, F., Ogden, A., Ordenovic, C., Osinde, J. O., Pagani, C., Pagano, I., Palaversa, L., Palicio, P. A., Pallas-Quintela, L., Panahi, A., Payne-Wardenaar, S., Peñalosa Esteller, X., Penttilä, A., Pichon, B., Piersimoni, A. M., Pineau, F. X., Plachy, E., Plum, G., Poggio, E., Prša, A., Pulone, L., Racero, E., Ragaini, S., Rainer, M., Raiteri, C. M., Ramos, P., Ramos-Lerate, M., Re Fiorentin, P., Regibo, S., Richards, P. J., Rios Diaz, C., Ripepi, V., Riva, A., Rix, H. W., Rixon, G., Robichon, N., Robin, A. C., Robin, C., Roelens, M., Rogues, H. R. O., Rohrbasser, L., Romero-Gómez, M., Rowell, N., Royer, F., Ruz Mieres, D., Rybicki, K. A., Sadowski, G., Sáez Núñez, A., Sagristà Sellés, A., Sahlmann, J., Salguero, E., Samaras, N., Sanchez Gimenez, V., Sanna, N., Santoveña, R., Sarasso, M., Schultheis, M., Sciacca, E., Segol, M., Segovia, J. C., Ségransan, D., Semeux, D., Shahaf, S., Sidiq, H. I., Siebert, A., Siltala, L., Silvelo, A., Slezak, E., Slezak, I., Snaith, O. N., Solano, E., Solitro, F., Souami, D., Souchay, J., Spagna, A., Spina, L., Spoto, F., Steele, I. A., Steidelmüller, H., Stephenson, C. A., Süveges, M., Surdej, J., Szabados, L., Szegedi-Elek, E., Taris, F., Taylor, M. B., Teixeira, R., Tolomei, L., Tonello, N., Torra, F., Torra, J., Torralba Elipe, G., Trabucchi, M., Tsounis, A. T., Turon, C., Ulla, A., Unger, N., Vaillant, M. V., van Dillen, E., van Reeven, W., Vanel, O., Vecchiato, A., Viala, Y., Vicente, D., Voutsinas, S., Weiler, M., Wevers, T., Wyrzykowski, Ł., Yoldas, A., Yvard, P., Zhao, H., Zorec, J., Zucker, S., and Zwitter, T. (2022). Gaia Data Release 3: A Golden Sample of Astrophysical Parameters. *arXiv e-prints*, page arXiv:2206.05870.
- Gaia Collaboration, Prusti, T., de Bruijne, J. H. J., Brown, A. G. A., Vallenari, A., Babusiaux, C., and Bailer-Jones, C. A. L. e. a. (2016). The Gaia mission. *A & A*, 595:A1.
- Gebran, M., Connick, K., Farhat, H., Paletou, F., and Bentley, I. (2022). Deep learning application for stellar parameters determination: I-constraining the hyperparameters. *Open Astronomy*, 31(1):38–57.
- Gebran, M., Farah, W., Paletou, F., Monier, R., and Watson, V. (2016). A new method for the inversion of atmospheric parameters of A/Am stars. *A & A*, 589:A83.
- Gebran, M., Monier, R., Royer, F., Lobel, A., and Blomme, R. (2014). Microturbulence in A/F Am/Fm stars. In Mathys, G., Griffin, E. R., Kochukhov, O., Monier, R., and Wahlgren, G. M., editors, *Putting A Stars into Context: Evolution, Environment, and Related Stars*, pages 193–198.
- Gill, S., Maxted, P. F. L., and Smalley, B. (2018). The atmospheric parameters of FGK stars using wavelet analysis of CORALIE spectra. *A & A*, 612:A111.
- Green, G. M., Rix, H.-W., Tschesche, L., Finkbeiner, D., Zucker, C., Schlaflly, E. F., Rybicki, J., Fouesneau, M., Andrae, R., and Speagle, J. (2021). Data-driven Stellar Models. *APJ*, 907(1):57.
- Heiter, U., Jofré, P., Gustafsson, B., Korn, A. J., Soubiran, C., and Thévenin, F. (2015). Gaia FGK benchmark stars: Effective temperatures and surface gravities. *A & A*, 582:A49.
- Hu, L., Chen, X., and Wang, L. (2022). Spectroscopic Studies of Type Ia Supernovae Using LSTM Neural Networks. *APJ*, 930(1):70.
- Hubeny, I. and Lanz, T. (1992). Accelerated complete-linearization method for calculating NLTE model stellar atmospheres. *A & A*, 262(2):501–514.
- Husser, T. O., Wende-von Berg, S., Dreizler, S., Homeier, D., Reiners, A., Barman, T., and Hauschildt, P. H. (2013). A new extensive library of PHOENIX stellar atmospheres and synthetic spectra. *A & A*, 553:A6.
- Jin-Meng, Y., Xiao-Qing, W., and min, Z. (2021). The regression of effective temperatures in apogee and lamost. *New Astronomy*, 86:101568.
- Kassounian, S., Gebran, M., Paletou, F., and Watson, V. (2019). Sliced Inverse Regression: application to fundamental stellar parameters. *Open Astronomy*, 28(1):68–84.
- Kjærsgaard, R. D., Bello-Arufe, A., Rathcke, A. D., Buchhave, L. A., and Clemmensen, L. K. H. (2021). Unsupervised Spectral Unmixing For Telluric Correction Using A Neural Network Autoencoder. *arXiv e-prints*, page arXiv:2111.09081.
- Kurucz, R. L. (1992). Atomic and Molecular Data for Opacity Calculations. *RMXAA*, 23:45.
- Li, T., Davies, G. R., Lyttle, A. J., Ball, W. H., Carboneau, L. M., and García, R. A. (2022a). Modelling stars with

- Gaussian Process Regression: augmenting stellar model grid. *MNRAS*, 511(4):5597–5610.
- Li, X., Wang, Z., Zeng, S., Liao, C., Du, B., Kong, X., and Li, H. (2022b). Estimation of stellar atmospheric parameters from LAMOST DR8 low-resolution spectra with $20 \leq \text{SNR} < 30$. *arXiv e-prints*, page arXiv:2204.06301.
- O'Malley, T., Bursztein, E., Long, J., Chollet, F., Jin, H., Invernizzi, L., et al. (2019). Kerastuner. <https://github.com/keras-team/keras-tuner>.
- Paletou, F., Böhm, T., Watson, V., and Trouilhet, J. F. (2015). Inversion of stellar fundamental parameters from ESPaDOnS and Narval high-resolution spectra. *A & A*, 573:A67.
- Paletou, F. and Zolotukhin, I. (2014). Using Virtual Observatory with Python: querying remote astronomical databases. *arXiv e-prints*, page arXiv:1408.7026.
- Perruchot, S., Bouchy, F., Chazelas, B., Díaz, R. F., Hébrard, G., Arnaud, K., Arnold, L., Avila, G., Delfosse, X., Boisse, I., Moreaux, G., Pepe, F., Richaud, Y., Santerne, A., Sottili, R., and Tézier, D. (2011). Higher-precision radial velocity measurements with the SOPHIE spectrograph using octagonal-section fibers. In Shaklan, S., editor, *Techniques and Instrumentation for Detection of Exoplanets V*, volume 8151 of *Society of Photo-Optical Instrumentation Engineers (SPIE) Conference Series*, page 815115.
- Petit, P., Louge, T., Théado, S., Paletou, F., Manset, N., Morin, J., Marsden, S. C., and Jeffers, S. V. (2014). PolarBase: A Database of High-Resolution Spectropolarimetric Stellar Observations. *PASP*, 126(939):469.
- Plez, B. (2012). Turbospectrum: Code for spectral synthesis. Astrophysics Source Code Library, record ascl:1205.004.
- Smalley, B. (2004). Observations of convection in A-type stars. In Zverko, J., Ziznovsky, J., Adelman, S. J., and Weiss, W. W., editors, *The A-Star Puzzle*, volume 224, pages 131–138.
- Smalley, B. (2005). T_{eff} and log g determinations. *Memorie della Societa Astronomica Italiana Supplementi*, 8:130.
- Straumit, I., Tkachenko, A., Gebruers, S., Audenaert, J., Xiang, M., Zari, E., Aerts, C., Johnson, J. A., Kollmeier, J. A., Rix, H.-W., Beaton, R. L., Van Saders, J. L., Teske, J., Roman-Lopes, A., Ting, Y.-S., and Román-Zúñiga, C. G. (2022). Zeta-Payne: A Fully Automated Spectrum Analysis Algorithm for the Milky Way Mapper Program of the SDSS-V Survey. *AJ*, 163(5):236.
- Tabernero, H. M., Marfil, E., Montes, D., and González Hernández, J. I. (2022). STEPARYN: A Bayesian code to infer stellar atmospheric parameters using spectral synthesis. *A & A*, 657:A66.
- Takeda, Y., Kawanomoto, S., Ohishi, N., Kang, D.-I., Lee, B.-C., Kim, K.-M., and Han, I. (2018). Photospheric carbon, nitrogen, and oxygen abundances of A-type main-sequence stars*. *Publications of the Astronomical Society of Japan*, 70(5):91.
- Ting, Y.-S., Conroy, C., Rix, H.-W., and Cargile, P. (2019). The Payne: Self-consistent ab initio Fitting of Stellar Spectra. *APJ*, 879(2):69.
- Tonry, J. and Davis, M. (1979). A survey of galaxy redshifts. I. Data reduction techniques. *AJ*, 84:1511–1525.
- Wu, J. (2017). Introduction to convolutional neural networks. *National Key Lab for Novel Software Technology. Nanjing University. China*, 5(23):495.
- Xiong, S., Li, X., and Liao, C. (2022). A Model RRNet for Spectral Information Exploitation and LAMOST Medium-resolution Spectrum Parameter Estimation. *arXiv e-prints*, page arXiv:2205.15490.
- Zorec, J., Frémat, Y., Domiciano de Souza, A., Royer, F., Cidale, L., Hubert, A. M., Semaan, T., Martayan, C., Cochetti, Y. R., Arias, M. L., Aidelman, Y., and Stee, P. (2017). Critical study of the distribution of rotational velocities of Be stars. II: Differential rotation and some hidden effects interfering with the interpretation of the $V \sin i$ parameter. *A & A*, 602:A83.
- Zorec, J. and Royer, F. (2012). Rotational velocities of A-type stars. IV. Evolution of rotational velocities. *A & A*, 537:A120.

A Tables

HIP	HD	T_{eff} (K)	T_{eff}^c (K)	T_{eff}^m (K)	$\log g$ (dex)	$\log gg^c$ (dex)	$\log g^m$ (dex)	[M/H] (dex)	[X/H] (dex)	[M/H] (dex)	$v_e \sin i$ (km/s)	$v \sin i^c$ (km/s)	$v \sin i^m$ (km/s)
HIP100108	HD193369	10109	7718	10100	4.08	4.30	4.29	0.14	0.04	0.04	120.4	102.0	110.0
HIP102098	HD197345	7081	7823	7572	2.22	2.51	2.13	0.61	0.06	0.48	31.3	34.7	34.7
HIP102208	HD199095	10610	8934	10500	4.03	3.95	3.95	0.03	0.0	0.00	27.4	32.0	30.0
HIP103298	HD199254	7842	8145	7900	3.37	4.01	3.50	-0.24	-0.2	-0.40	165.8	148.0	159.0
HIP104139	HD200761	9959	9595	10001	3.74	4.11	4.00	0.28	0.26	0.26	145.6	104.0	130.0
HIP106297	HD205117	10091	9370	9800	4.02	3.90	4.00	-0.10	0.00	-0.10	138.5	83.5	90.0
HIP10670	HD14055	10174	9340	10772	4.17	4.08	4.19	-1.31	-0.58	-1.20	233.2	246.0	240.0
HIP10793	HD14252	8638	8380	8749	3.35	4.74	3.40	-0.01	-0.05	0.00	23.5	22.0	25.0
HIP108875	HD209459	10307	10093	10350	3.16	3.55	3.48	-0.95	-0.15	-0.42	2.0	11.0	3.8
HIP109521	HD210715	8099	7901	8200	4.01	4.13	4.09	0.15	-0.10	-0.01	155.5	138.0	144.0
HIP111123	HD213320	10826	10125	10864	3.79	4.05	3.76	1.11	0.41	0.49	22.1	21.0	23.0
HIP111169	HD213558	9852	9197	9840	4.23	4.00	4.20	0.19	-0.28	0.00	149.1	128.0	150.0
HIP112029	HD214923	10396	11032	10723	3.26	3.87	3.50	-0.24	0.00	-0.30	189.6	162.0	185.0
HIP112051	HD214994	9834	9452	9866	3.67	3.68	3.65	1.44	0.08	0.42	5.1	10.0	5.0
HIP114745	HD219485	10361	9396	10000	3.81	3.82	3.81	0.05	0.00	0.03	25.5	23.0	25.0
HIP11484	HD15318	10790	10308	10900	3.64	4.00	3.48	0.00	-0.10	-0.04	61.7	57.0	65.0
HIP12706	HD016970	8587	8407	8551	4.29	4.18	4.30	-0.13	-0.01	-0.01	192.0	186.0	190.0
HIP1366	HD1280	8887	8697	8857	4.05	3.89	4.00	0.39	-0.69	0.14	101.9	102.0	102.0
HIP1473	HD1404	8728	8332	8770	4.17	4.18	4.17	0.28	-0.09	0.05	138.3	119.0	123.0
HIP15154	HD20149	9661	8631	9800	3.43	3.65	3.50	0.05	0.00	0.06	22.1	23.0	23.0
HIP16322	HD21686	10199	9468	10000	3.61	4.00	3.67	-0.22	-0.2	-0.40	237.9	244.0	244.0
HIP17791	HD23763	8581	8441	8591	4.33	4.03	4.10	0.33	-0.14	0.01	139.5	104.0	110.0
HIP18717	HD25175	10460	8034	10500	3.44	3.83	3.59	-0.10	-0.51	-0.16	56.9	55.0	55.0
HIP19194	HD26764	10123	8215	9825	3.57	3.39	3.67	-0.66	-0.65	-0.65	241.7	229.0	249.0
HIP20542	HD27819	8056	7957	8050	4.18	3.96	4.11	0.44	-0.07	0.20	50.1	42.0	43.3
HIP20542	HD27819	7799	7957	7800	3.67	3.96	3.70	0.13	-0.07	0.17	44.5	42.0	43.3
HIP20635	HD027934	7737	8105	7800	3.35	3.81	3.40	0.35	-0.01	0.05	84.0	85.0	85.0
HIP20901	HD28355	7170	7705	7592	3.95	4.00	3.97	0.23	0.30	0.20	89.9	105.0	90.0
HIP20901	HD028355	6823	7705	6262	3.23	4.00	3.22	0.13	0.30	0.20	92.7	105.0	92.8
HIP21029	HD28527	7466	8086	7700	3.58	3.91	3.69	0.09	0.13	0.10	66.1	86.0	70.0
HIP21589	HD29388	8120	8200	8000	3.64	3.88	3.69	0.27	-0.05	0.13	81.3	86.8	80.0
HIP21683	HD029488	7731	7947	7800	3.76	3.80	3.80	0.23	0.09	0.10	137.7	128.0	128.3
HIP21683	HD29488	7687	7947	7614	3.46	3.80	3.67	0.02	0.09	0.09	141.9	128.0	128.3
HIP23497	HD32301	7795	7863	7800	3.66	3.88	3.80	0.53	-0.01	0.15	130.4	124.5	131.0
HIP24340	HD33641	7536	7560	7560	3.96	3.92	3.96	0.19	-0.03	0.12	94.8	84.5	92.0
HIP29997	HD042818	10830	9370	10834	4.02	4.16	4.03	-0.57	0.30	0.30	265.6	255.0	260.0
HIP30060	HD043378	10278	9120	9580	4.13	4.10	4.15	-0.12	-0.30	-0.10	45.3	45.5	45.0
HIP32104	HD48097	10091	7508	9463	4.31	4.10	4.34	0.00	-0.10	-0.01	120.0	101.0	110.0
HIP32349	HD48915	9554	9900	9580	4.14	4.35	4.20	0.45	0.33	0.50	18.9	16.0	18.0
HIP32921	HD49098	10035	5685	10200	3.48	3.52	3.52	-0.34	-0.21	-0.35	154.2	117.0	140.0
HIP36145	HD58142	9340	9462	9266	3.30	3.67	3.55	0.12	0.00	0.00	21.0	18.6	19.0
HIP41152	HD070313	8747	8038	8720	4.05	4.00	4.03	0.46	-0.48	-0.01	119.1	112.0	114.0
HIP42028	HD72660	9160	9513	9200	3.66	4.00	3.60	0.26	0.10	0.21	4.1	9.0	5.0
HIP4436	HD5448	8163	7118	8222	4.29	3.81	4.20	0.24	-0.17	0.10	68.7	75.0	69.3
HIP45493	HD079439	6751	7630	7450	4.09	4.04	4.10	-0.46	-0.04	-0.5	175.4	159.0	159.0
HIP50448	HD88983	7628	7890	7600	3.73	3.89	3.89	-0.19	-0.19	-0.18	126.1	114.0	133.0
HIP50933	HD89822	9661	10000	9741	3.65	3.80	3.66	0.48	0.15	0.46	3.9	10.0	4.6
HIP51200	HD090470	8241	7845	8337	4.01	4.20	4.20	0.06	-0.01	-0.01	125.2	90.0	110.0
HIP52422	HD092769	7100	6990	7600	4.42	4.13	4.30	-0.48	-0.15	-0.60	223.7	207.0	212.0
HIP5310	HD006695	8773	8304	8720	3.99	4.30	3.91	0.07	-0.20	-0.01	164.2	149.0	150.0
HIP53485	HD94766	7927	7908	7917	4.56	4.06	4.21	0.12	-0.05	0.00	94.7	85.0	85.0
HIP54326	HD96399	7414	6662	7400	3.62	3.72	3.40	-0.39	-0.49	-0.40	78.0	70.0	70.0
HIP54425	HD96681	7963	7638	7829	3.41	3.66	3.40	-0.03	-0.14	-0.01	79.1	80.0	80.0
HIP55263	HD98377	8813	8297	8800	4.68	4.01	4.13	-0.11	-0.10	-0.10	55.3	50.0	50.0
HIP55542	HD69661	7578	7962	7597	3.74	3.64	3.80	0.51	-0.20	0.11	103.3	103.0	103.0
HIP55488	HD98747	7056	7136	6992	4.03	3.91	4.15	-0.47	-0.12	-0.20	39.0	35.0	35.0
HIP56429	HD100518	7942	7637	7986	3.60	3.61	3.50	-0.13	-0.16	-0.02	8.2	11.2	8.0
HIP57743	HD102841	7173	7400	7181	4.41	3.70	4.55	-0.28	-0.30	-0.30	123.5	90.0	90.0
HIP59223	HD106887	7823	8291	7900	3.93	4.20	3.80	0.46	0.21	0.21	86.2	82.0	84.1
HIP59988	HD106999	8109	6519	8116	4.14	4.07	4.12	0.05	-0.21	0.08	50.4	47.7	51.4
HIP60327	HD107655	9153	8607	9281	3.78	4.00	3.97	0.79	-0.09	0.08	56.1	46.0	50.0
HIP62874	HD112002	8045	7716	8000	4.15	3.99	4.00	0.11	-0.45	0.10	54.7	50.0	50.0
HIP65304	HD116379	7993	5848	8000	3.82	4.25	3.80	0.08	-0.27	-0.02	89.2	80.0	80.0
HIP65466	HD116706	8907	8480	8909	3.92	3.93	3.93	0.35	-0.20	-0.01	56.3	54.0	55.0
HIP6686	HD8538	7945	7980	7980	3.72	3.61	3.73	0.01	-0.45	-0.11	127.6	110.0	123.0
HIP67004	HD119537	8740	8661	8661	3.97	3.99	3.99	0.20	-0.44	0.03	17.9	13.5	16.4
HIP73156	HD132145	9434	9230	9376	3.95	4.13	4.00	-0.24	0.00	0.00	15.3	15.0	15.0
HIP75043	HD136729	8295	8247	8279	3.88	4.19	3.85	-0.33	0.09	-0.30	161.3	159.0	161.0
HIP76267	HD139006	10635	9515	10900	3.82	3.86	3.82	-0.26	0.20	-0.01	142.5	133.5	139.0
HIP78554	HD143894	9246	8652	9226	3.97	3.93	3.93	0.28	0.38	0.38	149.2	128.0	130.0
HIP79332	HD145647	9674	7645	9560	3.93	3.41	3.95	-0.40	-0.30	-0.36	46.8	43.0	45.0
HIP84036	HD155375	8704	8477	8700	4.49	4.06	4.08	0.40	0.20	0.22	28.1	27.9	28.0
HIP84821	HD157087	8592	8185	8600	3.38	3.10	3.44	0.11	-0.05	0.00	8.9	15.0	12.0
HIP85666	HD158716	8593	8068	8600	3.82	4.26	3.82	0.17	-0.13	0.00	5.1	15.0	6.0
HIP8903	—	8107	8352	8061	3.88	3.94	3.90	0.34	0.08	0.16	70.8	71.6	71.6
HIP91262	HD172167	9608	9485	9657	3.93	3.96	3.93	-0.51	-0.54	-0.50	23.2	23.0	23.0
HIP92396	HD174567	10395	9208	10500	3.46	3.55	3.50	0.44	0.00	0.15	9.6	15.0	12.0
HIP93526	HD176984	9876	8723	9880	3.40	3.47	3.44	-0.10	-0.14	0.00	28.9	24.2	30.0
HIP9480	HD012111	7586	7700	7700</									

Star ID	T_{eff} (K)	T_{eff}^c (K)	T_{eff}^m (K)	$\log g$ (dex)	$\log gg^c$ (dex)	$\log g^m$ (dex)	$[M/H]$ (dex)	$[X/H]^c$ (dex)	$[M/H]^m$ (dex)	$v_e \sin i$ (km/s)	$v \sin i^c$ (km/s)	$v \sin i^m$ (km/s)
HIP10138	5194	5188	5195	4.91	4.56	4.91	0.01	-0.23	-0.09	7.0	2.3	3.9
HIP102422	4937	4971	4940	2.54	3.40	2.99	0.30	-0.18	0.13	4.7	3.4	4.8
HIP105858	5909	6159	5910	3.47	4.35	3.92	-1.10	-0.67	-0.84	24.0	3.7	10.0
HIP10644	5871	5702	5845	3.92	4.29	3.92	-0.75	-0.43	-0.58	31.6	4.7	10.0
HIP10798	5186	5373	5286	4.52	4.61	4.53	-0.84	-0.47	-0.80	8.8	2.7	3.6
HIP109176	6664	6479	6693	3.72	4.23	4.02	-0.21	-0.10	-0.19	20.5	6.2	10.0
HIP110109	6106	5850	6019	3.74	4.39	4.13	-0.70	-0.21	-0.44	8.3	2.0	2.7
HIP114622	4755	4829	4749	2.12	4.50	2.59	0.92	0.05	0.20	9.0	2.0	8.0
HIP116771	6273	6186	6279	3.58	4.12	3.75	-0.30	-0.14	-0.27	11.1	6.7	10.0
HIP12777	6328	6264	6329	3.66	4.32	3.22	-0.16	-0.01	-0.15	12.6	8.9	10.2
HIP12843	5523	6371	6144	3.74	4.29	4.00	0.15	0.05	0.15	25.0	25.6	25.0
HIP13402	5171	5180	5170	4.54	4.56	4.55	0.62	0.08	0.21	9.9	4.9	10.0
HIP14632	6340	5963	6045	3.61	4.16	3.35	0.66	0.09	0.29	8.5	4.3	10.0
HIP14879	6160	6170	6165	3.50	3.95	3.57	-0.40	-0.21	-0.35	10.5	4.4	7.3
HIP15330	6071	5720	5854	4.28	4.53	4.30	-0.84	-0.22	-0.34	12.2	2.7	3.0
HIP15371	6155	5866	6066	3.96	4.48	4.22	-0.77	-0.23	-0.34	9.1	2.6	3.0
HIP15457	5908	5718	5908	3.60	4.50	4.33	-0.16	0.06	-0.16	10.4	5.2	8.0
HIP15510	6198	5401	6041	4.51	4.45	4.50	-0.52	-0.40	-0.49	7.0	1.5	4.0
HIP1599	6234	5957	6151	3.70	4.42	4.02	-0.43	-0.19	-0.45	16.4	3.0	15.0
HIP16537	5039	5084	5034	4.51	4.57	4.51	0.27	-0.11	0.06	16.9	2.5	15.0
HIP16852	6183	5997	6200	3.47	4.09	3.85	-0.21	-0.09	-0.21	8.3	4.3	8.0
HIP171	5853	5438	5798	4.40	4.38	4.40	-0.97	-0.79	-0.98	15.1	3.0	5.0
HIP17378	4734	5037	4750	2.35	3.77	3.27	0.36	0.10	0.25	24.7	2.3	15.0
HIP17420	4957	4979	4957	3.86	4.57	4.41	0.36	-0.11	0.10	9.4	3.0	5.7
HIP2021	6042	5848	5924	3.42	3.95	3.45	0.00	-0.09	0.00	9.2	3.3	5.0
HIP22263	6300	5834	6131	3.72	4.49	4.30	-0.48	0.01	-0.19	13.0	3.2	6.4
HIP22449	5857	6424	5820	3.52	4.29	3.77	0.02	0.00	0.02	18.3	17.2	18.5
HIP23311	4790	4790	4790	2.09	4.55	4.23	1.18	0.28	0.44	21.4	2.0	5.2
HIP23693	5838	6153	5727	3.66	4.44	4.06	-0.32	-0.17	-0.34	17.7	15.4	17.3
HIP24813	6167	5858	5979	3.67	4.20	3.98	0.51	0.05	0.26	3.7	2.0	3.1
HIP26779	5301	5243	5300	4.27	4.50	4.26	0.49	0.09	0.21	15.5	2.5	5.4
HIP27072	6381	6306	6384	3.64	4.31	3.99	-0.23	-0.05	-0.22	12.7	7.7	10.4
HIP27913	5892	5949	5895	3.74	4.44	4.21	-0.40	-0.03	-0.18	13.0	8.9	10.7
HIP29271	5628	5569	5621	3.70	4.43	4.20	0.77	0.10	0.25	18.4	1.8	2.3
HIP3093	5018	5221	5024	4.11	4.49	4.15	0.51	0.15	0.26	7.6	1.2	8.0
HIP37279	6770	6596	6775	3.47	4.00	3.74	-0.27	-0.01	-0.29	10.7	5.5	10.1
HIP37349	4812	4932	4826	2.74	4.60	4.68	0.83	-0.01	0.09	6.6	3.8	5.6
HIP3765	5024	4978	5020	4.82	4.61	4.82	0.06	-0.24	-0.04	9.7	2.0	6.3
HIP3821	6022	5925	6034	3.65	4.40	4.00	-0.59	-0.28	-0.60	10.5	2.8	9.2
HIP40693	5428	5402	5428	3.79	4.48	3.66	0.16	-0.03	0.14	9.0	2.0	6.7
HIP4148	4688	4952	4822	3.50	4.61	4.49	0.32	-0.11	0.00	8.7	1.8	4.5
HIP41926	5080	5243	5155	4.69	4.56	4.68	-0.73	-0.40	-0.48	8.8	2.7	6.8
HIP42438	5765	5876	5759	3.66	4.47	4.40	-0.35	-0.06	-0.29	13.8	10.0	13.2
HIP42808	5018	4969	5005	4.73	4.60	4.66	0.75	-0.03	0.10	8.9	3.8	9.6
HIP46853	6217	6336	6225	3.29	3.87	3.50	-0.42	-0.16	-0.31	12.3	8.6	10.0
HIP51459	6301	6156	6301	3.57	4.39	3.96	-0.32	-0.13	-0.28	9.3	4.3	10.0
HIP5336	5335	5316	5336	4.49	4.49	4.49	-1.15	-0.83	-0.98	19.3	5.4	15.0
HIP53721	6186	5882	6140	3.70	4.30	4.07	0.52	0.01	0.31	6.2	2.8	5.6
HIP544	5546	5481	5551	3.44	4.55	3.99	0.64	0.12	0.22	8.9	4.1	6.2
HIP56452	5128	5158	5129	4.80	4.56	4.68	-0.92	-0.38	-0.57	8.1	3.5	6.7
HIP56997	5605	5507	5609	3.71	4.54	3.45	-0.48	-0.05	-0.50	33.5	2.4	15.0
HIP57443	5982	5629	5970	4.21	4.44	4.21	-0.83	-0.29	-0.66	10.3	0.7	3.0
HIP57757	6470	6109	6246	3.55	4.10	3.86	0.52	0.13	0.33	8.3	4.0	10.0
HIP58576	5332	5532	5361	3.37	4.40	3.65	0.94	0.25	0.35	8.4	2.0	5.2
HIP61317	6063	5881	6061	3.70	4.39	3.38	-0.56	-0.19	-0.39	2.1	2.8	2.1
HIP61941	5502	6875	5433	3.64	4.26	3.88	-0.40	-0.09	-0.44	28.6	28.3	29.7
HIP64241	5687	6343	5250	3.64	4.09	3.99	0.01	-0.23	0.0	20.9	19.9	20.5
HIP64394	6517	6009	6225	3.72	4.40	4.24	0.06	0.04	0.06	10.7	4.4	10.0
HIP64924	5560	5558	5660	3.75	4.40	3.50	-0.17	-0.01	-0.13	8.4	2.2	8.0
HIP67927	6076	6047	6078	3.49	3.78	3.53	0.82	0.25	0.47	15.5	13.5	15.4
HIP68184	4776	4831	4792	2.20	4.55	4.38	1.00	0.12	0.33	25.4	1.3	9.0
HIP71681	5203	5551	5203	4.11	4.31	4.16	0.57	0.21	0.27	11.3	2.7	4.5
HIP72659	5616	5483	5595	4.23	4.56	4.37	-0.67	-0.14	-0.83	15.7	4.6	16.0
HIP72848	5290	5260	5291	4.10	4.53	4.11	0.60	0.08	0.14	9.5	4.5	6.3
HIP73695	6160	5495	6200	3.78	4.23	4.10	-0.54	-0.30	-0.42	6.2	3.7	3.7
HIP7513	6296	6155	6269	3.65	4.13	3.90	0.24	0.09	0.19	13.7	9.6	11.9
HIP77257	6206	5901	6131	3.57	4.15	4.00	-0.06	-0.01	-0.05	8.3	3.1	10.0
HIP7751	4969	5043	4970	4.58	4.63	4.61	-0.27	-0.20	-0.26	8.5	3.9	6.8
HIP77952	5492	7107	5377	2.77	4.16	3.76	0.11	-0.25	-0.20	79.2	75.0	75.0
HIP78072	6117	6278	6146	3.67	4.13	3.91	-0.36	-0.18	-0.32	13.9	10.0	11.9
HIP78775	5321	5294	5321	4.72	4.58	4.71	-0.85	-0.67	-0.76	6.6	2.0	7.0
HIP7918	6232	5880	6179	3.73	4.30	4.10	0.68	0.0	0.2	7.1	3.2	5.0
HIP79190	5033	5060	5024	4.91	4.55	4.66	-0.18	-0.37	-0.21	8.7	1.6	5.0
HIP79672	6213	5799	6053	3.71	4.43	4.16	-0.32	0.04	-0.29	8.3	2.5	8.3
HIP7981	5154	5201	5155	3.34	4.50	3.25	0.13	-0.04	0.12	10.4	1.7	10.0
HIP80337	6525	5882	6060	3.68	4.50	4.40	-0.30	0.03	-0.19	17.5	1.6	3.9
HIP80686	6417	6090	6459	3.68	4.45	4.24	-0.30	-0.08	-0.19	10.8	3.2	3.3
HIP8102	5456	5330	5459	4.57	4.51	4.57	-0.74	-0.52	-0.68	3.4	1.8	3.5
HIP81300	5087	5272	5080	4.15	4.57	4.39	0.07	0.02	0.07	8.0	2.0	4.1
HIP81693	5994	5764	5906	3.20	3.74	3.53	0.77	0.02	0.10	8.4	4.3	10.0
HIP8362	5257	5374	5257	3.56	4.54	4.30	0.01	0.05	0.01	7.2	1.3	10.0
HIP84405	5009	5089	5007	4.80	4.60	4.64	-0.48	-0.23	-0.38	7.7	2.5	5.1
HIP84720	5285	5209	5273	4.76	4.53	4.61	-0.77	-0.34	-0.46	8.6	1.9	4.5
HIP84862	6270	5703	6079	3.90	4.26	3.80	-0.70	-0.37	-0.79	2.9	1.7	3.0
HIP85235	5072	5290	5194	4.61	4.57	4.61	-0.74	-0.44	-0.52	5.0	1.3	3.4
HIP86036	6490	5893	6077	3.65	4.39	4.13	0.11	-0.03	0.08	13.5	4.5	6.0
HIP86400	4863	4883	4864	2.24	4.52	4.30	0.50	-0.08	0.17	13.7	2.5	4.1
HIP86974	5361	5508	5342	2.86	3.97	3.72	0.82	0.23	1.29	7.8	3.9	8.0
HIP88601	5174	5250	5182	3.82	4							